Carbohydrate Polymers 312 (2023) 120805

Contents lists available at ScienceDirect

Carbohydrate Polymers

journal homepage: www.elsevier.com/locate/carbpol

Influence of the cellulose purification process on the properties of aerogels obtained from rice straw

Pedro A.V. Freitas *, Consuelo González-Martínez, Amparo Chiralt

Institute of Food Engineering for Development, Universitat Politècnica de València, 46022 Valencia, Spain

ARTICLE INFO

Keywords:
Water absorbing material
Subcritical water extraction
Ultrasound-reflux heating
Alkaline treatment
Sorption isotherm

ABSTRACT

Cellulose aerogels were obtained from purified rice straw cellulose fibres (CF) by applying different extraction methods: the conventional alkaline treatment (ALK) and alternative aqueous extraction based on the ultrasound combined with reflux heating (USHT) and subcritical water extraction (SWE) (160 and 180 °C). The composition and properties of the CFs were significantly affected by the purification process. The USHT treatment was as efficient as the ALK at eliminating the silica content, but the fibres maintained a notable ratio of hemicellulose (~16 %). The SWE treatments were not so effective at removing silica (15 %) but greatly promoted the selective extraction of hemicellulose, especially at 180 °C (3 %). The CF compositional differences affected their hydrogel formation capacity and the properties of aerogels. A higher hemicellulose content in the CF led to better-structured hydrogels with better water-holding capacity, while the aerogels exhibited a more cohesive structure with thicker walls, higher porosity (99 %) and water vapour sorption capacity, but lower liquid water retention capacity (0.2 g/g). The residual silica content also interfered with the hydrogel and aerogel formation, giving rise to less structured hydrogels and more fibrous aerogels, with lower porosity (97–98 %).

1. Introduction

Aerogel consists of ultralightweight materials with outstanding physical and chemical properties, such as high porosity (80–99.8 %), low density (0.003–0.500 g.cm^{-3}) and a large surface area (100–1600 m^2.g^{-1}), as well as excellent optical and acoustic properties (Ferreira et al., 2021; Kistler, 1932; Long et al., 2018; Sun et al., 2021). Due to their unique properties, aerogels have great potential applications in different fields, including in the development of medical materials, optoelectronics, drug carriers, sensors, adsorption catalysis, acoustic and thermal insulation, aerospace materials, and superabsorbents for different applications (Jiang & Hsieh, 2014; Long et al., 2018; Zaman et al., 2020). A wide range of materials can be used for producing aerogels, such as synthetic polymers, carbon derivatives, inorganic compounds, macromolecules, and celluloses (Long et al., 2018). Cellulose aerogels in particular have been the subject of great interest in different research areas and for industrial applications, since they are highly porous materials with low density and a high water absorption capacity and are mechanically more resistant than other types of aerogels, such as those based on silica or metal oxides (Budtova, 2019; Jiang & Hsieh, 2014; Long et al., 2018). Likewise, cellulose aerogels have advantages when compared to other materials due to their biodegradability, renewability, non-toxicity, low cost, ready availability, and biocompatibility (Henschen et al., 2016; Wang et al., 2016). The process for manufacturing cellulose aerogels comprises dispersing or dissolving the cellulosic material to form wet cellulose hydrogels, followed by the solvent exchange, and then the drying step to remove the solvent and maintain the three-dimensional cellulosic structure (Zaman et al., 2020).

Cellulose is the most naturally abundant polymer and has long been a major renewable source of materials. In the native forms, the long poly (β-1,4-glucopyranose) chains are organised into highly crystalline 1.5–3.5 nm wide nanofibrils with intramolecular and intermolecular hydrogen bonds as part of larger microfibrils and macroscopic fibres (Habibi et al., 2010). Globally, Rice straw (RS) is the largest crop residue with relatively high cellulose content (about 40 %, Barana et al., 2016; Freitas et al., 2022a, 2022b) that could be used as a non-wood cellulose source. Cellulose fibres from mechanically ground rice straw were 12–35 nm wide and several micrometres long, with very similar crystal structures and mechanical properties to those obtained from grinding wood (Abe & Yano, 2009). Therefore, obtaining cellulose from rice straw to transform it into high-value-added products is an interesting

* Corresponding author.
E-mail address: pedvidef@doctor.upv.es (P.A.V. Freitas).

https://doi.org/10.1016/j.carbpol.2023.120805
Received 20 January 2023; Received in revised form 6 March 2023; Accepted 7 March 2023
Available online 11 March 2023

alternative in the context of the circular economy, while the use of a sustainable and eco-friendly process for this transformation is necessary. Different green alternatives and approaches for the valorisation of RS have been proposed, such as obtaining bioactive extracts (Freitas et al., 2020), paper production (Nagpal et al., 2021), biodiesel (Sahu, 2021), active packaging (Freitas et al., 2022a, 2022b), and cellulose fibres and nanofibres as reinforcing agents (Freitas et al., 2021). The use of rice straw, as a lignocellulosic waste, to obtain cellulosic aerogels represents a challenge, compared with the use of more refined cellulosic materials, but is an interesting valorisation strategy. Fontes-Candia et al. (2019) produced cellulose aerogels from *A. donax* waste biomass, with different degrees of purification, which exhibited a low density and excellent water and oil absorption and retention capacities.

Cellulose purification from the lignocellulosic rice straw complex is difficult (Chen et al., 2011) and requires the extraction of hemicellulose, lignin, and silica from the plant matrix. The most common step in the cellulose purification process is alkaline extraction, using KOH or NaOH solutions. This treatment chemically eliminates a substantial fraction of the hemicellulose, lignin, silica, and waxes present in the biomass (Zhang et al., 2014). After the alkaline treatment, a bleaching step is applied, until the colour of the cellulose fibre became off-white. The alkaline treatment presents two drawbacks: the use of non-environmentally-friendly solutions that need effluent processing and large amounts of washing water after treatment. More eco-friendly extraction methods, such as subcritical water extraction (SWE) or ultrasound-assisted aqueous extraction (UAE), could be used to replace the alkaline treatment of biomass.

SWE is an eco-friendly and cost-effective extraction technique based on the use of liquid water at high temperatures and at a pressure below the critical point (Castro-Puyana et al., 2013). In these subcritical processing conditions, an improved mass transfer is achieved, with greater solubilisation of compounds, due to the changes in the water properties. Water under subcritical conditions exhibits a decrease in dielectric constant, surface tension, density, and viscosity, as a function of temperature, which enhances its ability to penetrate into the solid matrix and solubilise less polar compounds (Ong et al., 2006; Plaza et al., 2010), which lends great potential in the extraction of non-cellulosic components from lignocellulosic residues.

The application of a combined ultrasound-reflux heating treatment to extract compounds from the lignocellulosic plant tissue was also very effective at purifying the cellulose fraction of rice straw (Freitas et al., 2022a, 2022b). The acoustic cavitation phenomena provoked by the ultrasound step led to the disruption of the plant cell structure, exposing the innermost plant tissues, and thereby improving the accessibility of the extracting solvent. Consequently, the extraction efficiency was enhanced by weakening intermolecular interactions between the plant matrix and non-cellulosic components. The fibres obtained were richer in hemicellulose but exhibited a similar reinforcing capacity in different polymer films (Freitas, 2023; Freitas et al., 2021; Freitas et al., 2022a, 2022b) to those obtained by alkaline extraction.

The aim of this study was to produce cellulose aerogels with CF obtained from RS by applying different purification methods, before the bleaching step: the usual alkaline treatment, a combined ultrasound-reflux heating method (USHT), and SWE at two processing temperatures (160 and 180 °C). The fibres were characterised as to their chemical composition, structural characteristics, and hydrogel-forming capacity. Likewise, cellulose aerogels were obtained by the freeze-drying of hydrogels and evaluated as to their microstructure, density and porosity, moisture sorption and water absorption and retention capacity.

2. Materials and methods

2.1. Materials and plant preparation

RS (*Oryza sativa* L.), *J. Sendra* var. was collected in the L'Albufera rice paddy (Valencia, Spain) and dried at 50 ± 2 °C under vacuum (0.8 mmbar) for 16 h. Afterwards, the plant material was ground (IKA, model M20, IKA Werke GmbH & Co. KG, Staufen, Germany) for 3 cycles of 90 s each, sieved (particles of under 0.5 mm), and then stored in airtight glass bottles, to prevent sample hydration, at 20 ± 2 °C until further use.

Acetic acid, magnesium nitrate ($Mg(NO_3)_2$), and di-phosphorus pentoxide (P_2O_5) were purchased from PanReac Quimica S.L.U. (Castellar del Vallés, Spain). Sodium acetate trihydrate was purchased from FlukaTM (Germany). Sulfuric acid (98 % purity), sodium hydroxide, glucose, arabinose, and sodium chlorite were supplied by Sigma-Aldrich (St. Louis, MO, USA). D(+)-Xylose was supplied by Merck KGaA (Darmstadt, Germany).

2.2. Obtaining cellulosic fractions

Three alternative treatments were applied before the bleaching step to the ground RS to remove the hemicellulose and lignin components: 1) the traditional alkaline treatment, as a control; 2) the combined ultrasound-reflux heating method; and 3) subcritical water extraction.

2.2.1. Alkaline treatment

The alkaline extraction of RS was performed as previously described by Collazo-Bigliardi, Ortega-Toro, Chiralt Boix (2018a, 2018b). A dispersion consisting of RS (5 % wt.) and sodium hydroxide solution (4.5 % wt.) was heated to 100 °C using a typical reflux device for 2 cycles of 3 h each. At the end of each cycle, the solid material was filtered and washed with abundant water to remove the alkaline solution. Finally, the insoluble residue obtained (ALK) was dried at 35 °C for 24 h to determine the step yield.

2.2.2. Combined ultrasound-reflux heating method

A sequential method consisting of a combination of ultrasound and reflux heating was performed according to Freitas et al. (2022a, 2022b). Briefly, a 5 % (w/v) aqueous dispersion of RS was first sonicated at 25 °C (by immersion in an ice bath) for 30 min, using a probe high-intensity ultrasonic homogeniser (Vibra Cell™ VCX750, 750 W power, Sonics & Material Inc., Newtown, CT, USA) operating at a frequency of 20 kHz, 40 % sonication amplitude, in continuous mode. Afterwards, the plant dispersion was heated at reflux (100 °C) for 1 h, filtered and washed with water three times and the insoluble fraction (USHT) was dried at 35 °C for 24 h to determine the step yield.

2.2.3. Subcritical water extraction

The subcritical water extraction (SWE) of the RS was carried out using an RS: distilled water ratio of 1:10 (*w/v*). The SWE process was performed using a Pressure Reactor (Model 1-T-A-P-CE, 5 L capacity, Amar Equipment PVT. LTD, Mumbai, India) under two extraction conditions selected on the basis of the optimized xylan yields reported for rice husk (Requena et al., 2019): 160 °C, 7 bars, 150 rpm, for 30 min; and 180 °C, 11 bars, 150 rpm for 30 min. Afterwards, the plant dispersion was cooled to 30 °C, filtered with a qualitative filter (Filterlab), and washed with water to eliminate the soluble fraction retained in the solid residue. Then, the insoluble fractions (named as SWE-160 and SWE-180) were dried at 35 °C for 24 h to determine the step yield.

2.2.4. Bleaching treatment

The solid residues (ALK, USHT, SWE-160, and SWE-180) were bleached according to Freitas et al. (2022a, 2022b). The dry samples were mixed at 5 % wt. with a bleaching solution prepared by mixing equal parts of distilled water, acetate buffer solution (2 N), and sodium chlorite (1.7 %, w/v). The suspension was treated under reflux heating at 100 °C for 4 h. Thereafter, the solid fraction was filtered and washed with distilled water to remove the residual bleaching solution. The procedure was repeated three times. Then, the bleached samples were dried at 35 °C for 48 h and milled using a milling machine (model M20, IKA Werke GmbH & Co. KG, Staufen IKA, Germany), applying pulses of

2 s for 20 min. The bleached solid residues were labelled as ALK—B, USHT-B, SWE-160-B, and SWE-180-B.

2.3. Characterization of cellulosic fractions

2.3.1. Chemical composition

The chemical composition of the different lignocellulosic fractions, typically cellulose, hemicellulose, and lignin were determined following the standard NREL methodology (NREL/TP-510-42,618) (Sluiter, 2008b). Before the hydrolysis, the raw RS and the non-bleached solid residues from the different treatments were submitted to water extraction following the standard NREL method to determine water extractives of biomass (NREL/TP510-42,619) (Sluiter, 2008a). After the two-step sulfuric acid hydrolysis, the Klason lignin content was determined gravimetrically as the acid-insoluble fraction, while the sugar composition in terms of glucose, xylose, and arabinose was quantified in the acid-soluble fractions by high-performance liquid chromatography (HPLC). To this end, a liquid chromatograph (Agilent Technologies, model 1120 Compact LC, Germany) equipped with a HILIC Luna Omega Sugars column (150 mm × 4.6 mm, 3 μm) and an evaporative light scattering detector (ELSD Agilent Technologies 1200 Series, Germany) was used. The mobile phase was water: acetonitrile (25:75), in isocratic mode, at a flow rate of 0.8 mL.min^{-1}. The detector conditions were: 40 °C, 3.0 bars of nitrogen pressure, and a gain of 5. The data were analysed by the software ChemStation Program (Agilent Technologies, Germany). The hemicellulose content was calculated by the sum of the xylose and arabinose contents with respect to the initial solid fraction, and the cellulose content was obtained from the glucose concentration. The ash content of the cellulosic fractions was determined from the thermogravimetric analyses, described below.

2.3.2. Colour properties

The colour properties of the bleached CFs were obtained by evaluating the colour coordinates of cellulosic films (Section 2.4) in order to avoid the porosity effect, following the Kubelka-Munk theory of multiple scattering using a spectrocolorimeter (CM-3600d, Minolta Co., Japan) (Freitas et al., 2021). The reflection spectra of the films were obtained from 400 to 700 nm using white and black backgrounds. Then, the colour coordinates L^* (lightness), a^* (redness-greenness), and b^* (yellowness-blueness) were calculated from the infinite reflectance spectra, using D65 illuminant and 10° observer. The psychometric coordinates, (C_{ab}^*) (Eq. (1)) and hue angle (h_{ab}^*) (Eq. (2)) were calculated from a^* and b^* values. The whiteness index (*WI*) of the samples was also determined following Eq. (3). The measurements were taken in triplicate for each sample and three times in each replicate.

$$C_{ab}^{*} = \sqrt{a^{*2} + b^{*2}} \tag{1}$$

$$h_{ab}^{*} = \operatorname{arctg}\left(\frac{b^{*}}{a^{*}}\right) \tag{2}$$

$$WI = 100 - \sqrt{(100 - L^{*})^{2} + a^{*2} + b^{*2}} \tag{3}$$

2.3.3. Microstructure

A Field Emission Scanning Electron Microscope (ULTRATM 55, Zeiis, Oxford Instruments, UK) was used to evaluate the morphologies of the raw RS and the different cellulosic fractions obtained in the cellulose extraction steps. Conditioned samples (P_2O_5 at 25 °C for two weeks) were previously covered with a platinum layer using an EM MED020 sputter coater (Leica BioSystems, Barcelona, Spain) for 30 s, and the images were taken at 2.0 kV acceleration voltage.

2.3.4. Thermogravimetric analysis

The thermal behaviour of the different lignocellulosic fractions was evaluated by thermogravimetric analysis (TGA) using a thermogravimetric analyser (TGA 1 Stare System analyser, Mettler-Toledo, Switzerland) under nitrogen flow (10 mL.min-1). Samples (conditioned in P_2O_5 at 25 °C for two weeks) of about 3–5 mg were weighed in alumina pans and heated from 25 to 700 °C at 10 °C.min^{-1}. The thermogravimetric curves and their derivatives (DTGA) were analysed to obtain the initial (T_{on}) and the maximum thermo-degradation rate (T_p) temperatures and the residual mass for each observed thermal event, as well as the final residue. These measurements were taken in duplicate.

2.3.5. Fourier transformed infrared spectroscopy (FTIR)

FTIR spectra of the lignocellulosic fractions at different purification steps were evaluated using an FTIR spectrometer (Vertex 80, Bruker AXS GmbH, Karlsruhe, Germany) equipped with microscopic (Hiperion) and attenuated total reflectance accessories. Spectra were obtained at a resolution of 6 cm^{-1}, in the wavelength range of 4000–650 cm^{-1}, performing 128 scans for each spectrum.

2.3.6. X-ray diffraction analysis (XRD)

An X-ray diffractometer (AXS/D8 Advance, Bruker, Karlsruhe, Germany) was used to evaluate the X-ray diffraction pattern spectra of the different cellulosic fractions. The conditioned samples were compacted to cover the sample holder and the analysis was performed using Kα-Cu radiation (λ: 1.542 Å), 40 kV, 40 mA, step size of 2.0°. min^{-1}, and a 2θ scanning angle of between 5° and 40°. The crystallinity index (*CI*), expressed as a percentage, was determined from the maximum intensity of 200 lattice diffraction (I_{200}, crystalline peak) and the diffraction intensity at $2\theta = 18°$ ($I_{2\theta\ 18°}$, amorphous phase valley) using the empirical equation (Eq. (4)) proposed by Seagal et al. (1959).

$$CI\ (\%) = \frac{(I_{200} - I_{2\theta\ 18})}{I_{200}} \times 100 \tag{4}$$

2.3.7. Hydrogel formation capacity

The ability of each cellulosic fraction to form hydrogels through cyclic freezing-thawing (FT) was also evaluated. To this end, CF samples (0.075 g) were dispersed with 15 mL of distilled water and ultrasonicated (Vibra CellTM VCX750, Sonics & Material, Inc., Newtown, CT, USA) to promote cellulose defibrillation (Xiao et al., 2015). Operating conditions in a continuous mode were 20 kHz frequency and 40 % sonication amplitude, at 25 °C (using an ice bath to prevent heating), for 20 min. Then, CF dispersions were placed in polycarbonate centrifuge tubes (Beckman Coulter Inc., USA) and submitted to three cycles of FT. Each cycle consisted of freezing at −20 °C for 16 h and subsequent thawing at room temperature for 9 h. After each FT cycle, the morphology (consistency and syneresis) of the formed hydrogels was visually analysed and photographs were taken.

2.4. Production of aerogels

Cellulosic aerogels were obtained following Fontes-Candia et al. (2019), with some modifications. Briefly, water dispersions of CF samples were prepared as described in Section 2.3.7 and poured into a Petri dish 6 cm in diameter, frozen at −40 °C for 16 h, and then freeze-dried (Telstar, model LyoQuest-55) at −60 °C, 0.8 mbar for 72 h. The aerogels obtained were labelled as USHT-B, ALK—B, SWE-160-B, and SWE-180-B, according to the respective extraction process applied.

Cellulose films were also obtained from the CF aqueous dispersions by casting 15 mL in Petri dishes (6 cm diameter) and drying at 25 °C for 72 h. Density of these films were determined and used to calculate the aerogel porosity as described in next section. These films were also used to measure the colour of the CFs, avoiding the effect of fibre packing.

Before characterisations, both aerogels and films were conditioned in a desiccator containing P_2O_5 (0 % RH) at 25 °C.

2.5. Characterization of aerogels

2.5.1. Density and porosity

The density of the different aerogels and films was determined considering the mass and volume of each sample. The sample dimensions were measured using a digital calliper (Palmer, model COMECTA, Barcelona, accuracy of 0.001 mm) at six different positions in each replicate (four samples per treatment). The theoretical and measured porosity of the aerogels were determined by means of Eqs. (5) and (6), respectively, where ρ_a is the aerogel density, ρ_c is the theoretical density of cellulose (1676 mg.cm^{-3}; Diddens et al., 2008), and ρ_f is the density of the cellulosic films.

$$\text{Theoretical Porosity } (\%) = \left(1 - \frac{\rho_a}{\rho_c}\right) \times 100\% \quad (5)$$

$$\text{Measured Porosity } (\%) = \left(1 - \frac{\rho_a}{\rho_f}\right) \times 100\% \quad (6)$$

2.5.2. Microstructure

The micrographs of the aerogel surfaces were obtained as described in Section 2.3.5 using samples 1 cm × 1 cm in size, coated with platinum for 1 min. The images were taken at 2.0 kV acceleration voltage.

2.5.3. Sorption isotherms

Conditioned (0 % RH at 25 °C) aerogel samples were placed in desiccators at 25 °C containing different over-saturated salt solutions (LiCl, CH_3COOK, $MgCl_2$, K_2CO_3, KI, NaCl, and KCl) with water activities (a_w) of 0.113, 0.2251, 0.3278, 0.4316, 0.6886, 0.7529, and 0.8434, respectively. The samples were periodically weighed and when these reached constant weight, the equilibrium moisture content was determined from the gained water mass and the initial moisture content of each sample, determined by TGA. The sorption experimental data were fitted to the Guggenheim-Anderson-de Böer (GAB) (Eq. (7)) model using the Excel and the OriginPro programs (Version 2021, OriginLab Corporation, Northampton, MA, USA).

$$\omega_e = \frac{\omega_0 \bullet C \bullet k \bullet a_w}{(1 - k \bullet a_w) \bullet [1 + (C - 1) \bullet k \bullet a_w]} \quad (7)$$

Where ω_e is the equilibrium moisture content (dry basis), ω_0, the monolayer moisture content, a_w, the water activity and k and C are the equation parameters, which are temperature dependent and related to the water sorption enthalpy.

BET molecular model of adsorption (Eq. (8)) was also fitted for $a_w <$ 0.4 to the different sorption data in order to determine the specific surface area (SSA = 3.5 × 10^3 ω_0) of the aerogels from the determined monolayer moisture content (ω_0).

$$\omega_e = \frac{\omega_0 \bullet C \bullet a_w}{(1 - a_w) \bullet [1 + (C - 1) \bullet a_w]} \quad (8)$$

2.5.4. Water absorption and retention capacities

The water absorption capacity (WAC) of the aerogels, expressed as g absorbed water. g^{-1} aerogel, was measured according to what was previously described by Jiang and Hsieh (2014), with some modifications. Briefly, conditioned aerogel samples (P_2O_5 at 25 °C), 1 cm × 1 cm in size, were placed on a mesh and immersed in a Petri dish containing distilled water (30 mL) at 20 °C for 15 min (enough time to saturate). Afterwards, the excess of water contained in the mesh was removed with absorbent paper and the system was weighed. The measured WAC was determined by applying Eq. (9), where w_s and w_o are the masses of the fully water-saturated aerogels and dried aerogels, respectively. The theoretical WAC was also calculated, assuming a constant aerogel volume and considering the determined porosity and the aerogel and water densities (ρ_w = 0.9982 g.cm^{-3} at 20 °C) (Eq. (10)). To determine the water retention capacity (WRC), the system containing the saturated aerogel was placed on absorbent paper and periodically weighed until reaching a constant weight. The WRC was expressed as the mass of water retained per mass unit of aerogel. All these analyses were performed in quintuplicate for each aerogel.

$$\text{Measured WAC} = \frac{(w_s - w_o)}{w_o} \quad (9)$$

$$\text{Theoretical WAC} = \frac{\text{Porosity} \times \rho_{water}}{\rho_a} \quad (10)$$

2.6. Statistical analysis

The experimental data obtained were analysed through analysis of variance at a confidence level of 95 % using Minitab Statistical Program (version 17). Tukey's HSD (honestly significant difference), considering the least significant difference (α) of 5 %, was performed to determine whether there were significant differences between the formulations.

3. Results and discussion

3.1. Properties of cellulosic fractions

3.1.1. Yield, composition, appearance, and colour properties

Fig. 1 shows the samples obtained during the cellulose purification processes by applying the different pre-treatments before and after the bleaching step. The bleached CFs obtained with the alkaline treatment and the combined ultrasound-reflux heating method exhibited similar appearance and whiteness, as also reported by Freitas et al. (2022a, 2022b), whereas the CFs from the SWE method had a more yellowish appearance, especially the sample obtained at 180 °C that exhibited a more vivid and intense colour. This was also reflected in the colour coordinates and whiteness index (*WI*) of cellulosic films (Table 1) obtained from the bleached samples, which were used to evaluate colour instead of cellulose fibres to avoid the porosity effects. ALK-B fibre gave rise to films that were whiter, less saturated in colour and with higher lightness values than the other cellulose fractions. Films prepared with the USHT-B fibres exhibited intermediate colour coordinates and *WI*, while those prepared with the SWE fibres were more yellowish with the most saturated colour and the lowest *WI* ($p < 0.05$), especially in the case of the treatment at 180 °C. The presence of coloured compounds in the SWE fibres suggested that the cellulose purification process could not be as efficient as the other methods. The partially degraded compounds of residual lignin and the newly formed brown compounds during the hydrothermal process seems to be more linked to the cellulose fibres and were not so efficiently removed by the bleaching step. The high temperatures used in the subcritical extraction step partially depolymerise cellulose and hemicellulose chains, thus favouring browning reactions, such as caramelisation or Maillard reactions, as described by other authors (Plaza et al., 2010). This agrees with the appearance of the solid residues after the SWE step (SWE-160-B and SWE-180-B; Fig. 1), which were darker than those obtained with the alkaline or the combined ultrasound-reflux heating treatments.

To investigate the differences between the cellulose purification processes, the yields (with respect to the dried RS), water extractables, as well as chemical composition in terms of cellulose, hemicellulose, klason lignin, and ashes, were analysed and shown in Table 2. The obtained composition of raw RS was coherent with those found by other authors (Barana et al., 2016). In general, an enrichment in cellulose content was observed after each purification step, especially after the bleaching treatment (Table 2), which points to the different extent to which hemicellulose and lignin are eliminated and the solubilisation/hydrolysis of silica, which is present in large quantities in the raw RS (~17 % wt., Zhang et al., 2014). The fractions from the alkaline treatment (ALK and ALK—B) exhibited the lowest yields, thus indicating that this treatment was the most efficient at removing the non-cellulosic

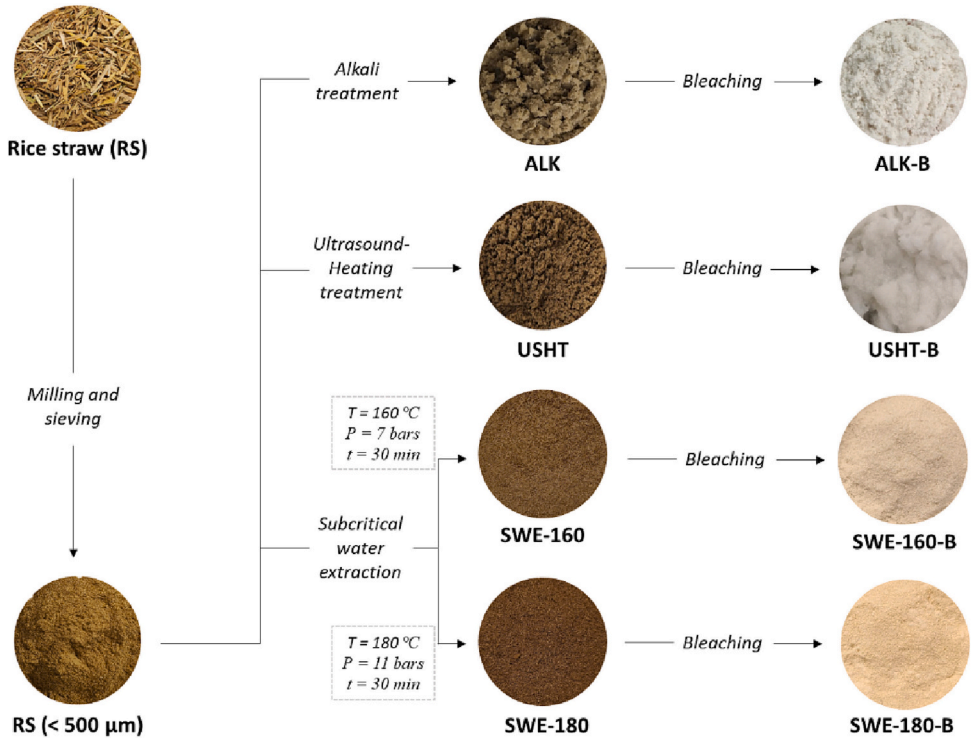

Fig. 1. Flow chart and samples obtained in the purification process steps (extraction and bleaching) applied on RS.

Table 1
Colour coordinates and whiteness index (*WI*) of the cellulosic fibres obtained by the different purification treatments (determined in the cast films to avoid the porosity effects).

Treatment	*L**	*C**	*h**	*WI*
ALK-B	93.0 ± 1.4^{a}	2.8 ± 0.4^{d}	75 ± 3^{c}	92.4 ± 1.2^{a}
USHT-B	88.5 ± 0.7^{b}	4.4 ± 0.4^{c}	98 ± 1^{a}	87.7 ± 0.5^{b}
SWE-160-B	88.2 ± 0.7^{b}	5.8 ± 0.1^{b}	95 ± 1^{ab}	86.8 ± 0.6^{bc}
SWE-180-B	87.8 ± 0.2^{b}	6.5 ± 0.4^{a}	94 ± 1^{b}	86.1 ± 0.5^{c}

Different subscript letters in the same column indicate significant differences by means of the Tukey test ($p < 0.05$).

components from RS. This was also reflected in the fact that the fractions had the lowest hemicellulose, lignin, and silica content. The USHT and SWE treatments led to samples with a similar cellulose content (36–40 %), which significantly increased ($p < 0.05$) after the bleaching step (62–69 %).

SWE promoted a selective extraction of hemicellulose, especially at 180 °C, but a high ratio of ash/silica (~15 %) was maintained even after the bleaching step. In fact, the SWE-180 treatment was more effective at eliminating hemicellulose than the alkaline treatment (3 % vs. 10 % in the bleached fibres). This could be related to a better capacity of the SWE to partially solubilise or hydrolyse the hemicellulose chains, with the formation of arabinoxylan oligomers, as reported by other authors (Ong et al., 2006; Plaza et al., 2010). In contrast, the solubilisation of silica did not occur quantitatively in SWE processes. This is highly dependent on temperature and pH, solubilising at high temperatures and pH above 9.0 (Le et al., 2015). At the pH of SWE conditions, silica was not extracted, whereas it was almost completely eliminated during the alkaline treatment. The USHT-B samples had a similar ash content to that ALK—B, which indicates that this treatment was mechanically efficient at removing silica (~58 % wt. reduction). In fact, the sonication of plant suspensions has been proposed as an effective method in biomass desilification to avoid the operational problems that silica particles present in biorefineries (Le et al., 2015; Yunus et al., 2010). During the bleaching step, an additional lixiviation of silica occurred in the ALK and USHT samples, which could be attributed to the weakening of the lignocellulosic matrix and the increase of the matrix exposure area provoked by the previous treatments. Of the different forms of silica identified in rice husk (silanediol groups [(OH)2*Si(OSi)2], silanol groups [(OH)*Si(OSi)3], and silicon-oxygen tetrahedral frameworks

Table 2
Yield (with respect to the initial mass of RS), water extractables, and composition of the untreated RS and the cellulosic fractions at the different purification steps (mean values ± standard deviation).

Sample	Yield (% wt.)	Water extractables (% wt.)	Cellulose (% wt.)	Hemicellulose (% wt.)	Klason Lignin (% wt.)	Ashes (% wt.)
RS	–	9.3 ± 0.8^{c}	36.7 ± 0.4^{f}	19.3 ± 0.1^{a}	21.2 ± 0.5^{bc}	17 ± 2^{a}
ALK	31.2	2.4 ± 0.4^{d}	54.6 ± 3.1^{d}	8.2 ± 1.2^{c}	6.6 ± 1.7^{d}	8 ± 1^{bc}
USHT	80.1	14.8 ± 0.1^{a}	40.3 ± 0.8^{e}	20.1 ± 1.2^{a}	19.7 ± 1.4^{c}	10 ± 2^{b}
SWE-160	79.5	15.5 ± 0.4^{a}	36.0 ± 0.2^{f}	14.2 ± 2.3^{b}	22.6 ± 0.2^{ab}	15 ± 1^{a}
SWE-180	75.2	12.3 ± 0.1^{b}	38.1 ± 2.0^{ef}	2.7 ± 0.1^{d}	23.7 ± 1.5^{a}	13 ± 5^{ab}
ALK-B	29.5	n/a	73.4 ± 2.1^{a}	10.1 ± 0.8^{c}	2.6 ± 0.4^{e}	2 ± 3^{cd}
USHT-B	37.4	n/a	65.9 ± 0.7^{b}	15.6 ± 0.4^{b}	5.2 ± 0.2^{d}	7 ± 2^{bc}
SWE-160-B	35.0	n/a	61.6 ± 0.1^{c}	9.7 ± 1.3^{c}	4.7 ± 0.6^{de}	15 ± 1^{a}
SWE-180-B	39.2	n/a	68.7 ± 1.4^{b}	3.4 ± 0.4^{d}	5.1 ± 1.1^{d}	15 ± 3^{a}

Different subscript letters in the same column indicate significant differences by means of the Tukey test ($p < 0.05$).

[*Si(OSi)4]), the silanediol and silanol amorphous forms represent about 70 % and can partially dissolve in aqueous media (Mochidzuki et al., 2001), such as bleaching solution, if these are not bonded to the cellulose matrix. These Silica forms in the SWE treated samples could be to more strongly bonded to cellulose fibres since these were not leached during the bleaching step. This bonding could occur through similar mechanisms described for the cellulose hydrophobization with silane coupling agents (Cabrera et al., 2016).

Of the proven alternative methods, SWE at 180 °C was the most efficient at purifying the cellulose fibres since this exhibited a cellulose content closer to that of the alkaline method. This was due to its greater hemicellulose extractive power, despite its inability to remove the silica.

3.1.2. Microstructure of CFs

The morphological changes in the insoluble RS fractions provoked by the different CF purification methods are shown in Fig. 2. Rod-shaped RS fragments demonstrate the typical morphological nature of the plant tissue, a porous material composed of highly silicified epidermis, parenchyma and vascular tissues, and lumen (Jiang & Hsieh, 2014; Le et al., 2015).

After the alkaline treatment of the raw RS, distorted particles (inserts at 100× magnification in Fig. 2, ALK) with a homogeneous surface could be observed, which can be related to the elimination of hemicellulose, silica, and waxes. Micrographs of RS treated with the USHT combined method revealed disrupted and deformed structures caused by sonication, thus exposing the innermost parts of the RS matrix. Quite a similar effect was observed in the micrographs of the SWE fractions, although these showed a rougher surface, with the presence of small particles, indicating that the silica or lignin were still present in the lignocellulosic structure (Abd-Talib et al., 2020). The morphology of bleached fibres revealed a smoother structure due to the removal of a substantial fraction of the lignin, thus better exposing the cellulose fibre bundles. The appearance of the CFs was similar, with diameters of <5 μm, as also reported by Jiang et al. (2013). Defibrillated CFs were observed in the bleached samples for all of the treatments, thus indicating the effectiveness of the combined ultrasound-reflux heating and SWE methods at eliminating non-cellulosic components. A smaller quantity of defibrillated fibres was detected in the SWE-180-B samples, which may be related to the large amount of hemicellulose removed; this leads to more cellulose OH groups available for the establishment of hydrogen bonds, giving rise to more aggregated CF (Bochek, 2003).

3.1.3. TGA analysis

The changes in the thermal stability of the cellulosic fractions as the purification progressed were analysed by thermogravimetric analysis. Fig. 3 shows the mass loss and derivative curves of untreated RS and bleached fibres. The thermogravimetric parameters for each purification step, including the initial (T_{on}) and maximum degradation rate (T_p) temperatures, the weight loss at each step (Δm), as well as the final residual mass, are gathered in Table 3. All of the insoluble fractions showed a weight loss (4–5 %) below 150 °C, which is associated with the loss of adsorbed water, as also reported by other authors (Wu et al., 2013). In similar lignocellulosic materials, such as rice husk, hemicellulose, cellulose and lignin fractions exhibited typical thermal degradation patterns in temperature ranges of 150–350 °C, 275–350 °C, and 250–500 °C, respectively (Collazo-Bigliardi, Ortega-Toro, Chiralt Boix, 2018a, 2018b; Mansaray & Ghaly, 1998), but other studies reported a wider temperature rage in the case of lignin degradation (160–900 °C) with high residual mass (Yang et al., 2007) The degradation profile of the raw RS showed a broadened peak, with a marked shoulder, between 170 and 400 °C, mainly associated with the cellulose and hemicellulose degradation, followed by the final degradation of the lignin fraction from 400 to 550 °C. As the insoluble fractions became richer in cellulose, mainly after the bleaching step, the second event started at higher temperatures and the main peak narrowed while the initial shoulder disappeared, in agreement with the greater cellulose purity. Yang et al. (2007) reported that cellulose pyrolysis occurred between 315 and 400 °C, with the maximum weight loss rate at 355 °C and very little solid residue. The mass loss of the thermo-degradation step of the samples associated within cellulose degradation (170–400 °C in Table 3) significantly increased after the bleaching step due to the removal of other compounds and enrichment in cellulose while the peak temperature was barely modified. Thus, the ALK-B fibre, with the highest cellulose content (Table 2), exhibited the highest mass loss (Δm of 73 %) in this step, whereas the SWE-B samples presented the lowest values (Δm of 64 %) with the highest final residual mass, in agreement with the final cellulose, hemicellulose and silica contents of the samples.

All of the treatments exhibited a broadened peak between 380 and 660 °C, which is associated with either the final decomposition of lignin, which occurs at a very low mass rate, or with the final thermal degradation of hemicellulose, since no contribution of cellulose at $T > 400$ °C has been found (Yang et al., 2007). Thus, these results coincide with the composition data of the fibres and the lack of total efficiency of the purification methods to completely remove lignin, as also reported by El-Sakhawy and Hassan (2007).

3.1.4. FTIR and X-ray analysis

The vibrational pattern of the functional groups present in each cellulosic fraction and the changes induced by the different purification treatments were analysed by FTIR in the 4000–800 cm^{-1} region (Fig. 4a). The broad bell-shaped absorption band between 3000 and 3800 cm^{-1} is assigned as O—H stretching vibrations, when involved in hydrogen bonds (Do et al., 2020). In general, this band becomes more intense and narrower as the purification progresses, which is related to the removal of amorphous components, such as hemicellulose, lignin, and waxes (Freitas et al., 2022a, 2022b; Wang et al., 2018). This behaviour was mainly detected for the fraction treated with the alkaline solution and the corresponding bleached ALK-B fibre. The band at 1730 cm^{-1} is attributed to the stretching of the C═O present in phenolic acids and uronic acids from the lignin and hemicellulose components, respectively (Chen et al., 2011; Esteves et al., 2013). Except for the ALK fraction (bleached or not), this peak is present in every treatment, indicating the greater efficiency of the alkaline method at eliminating non-cellulosic components. The peak at 1511 cm^{-1} in the FTIR spectra of the untreated RS and USHT, SWE-160, and SWE-180 fractions is associated with the C═C stretching vibration of aromatic rings present in the lignin structure (Xu et al., 2006). This band disappeared in all of the spectra of the bleached samples, coherent with the reduction in lignin content (Table 2).

For the treatments submitted to SWE, the absorption band at 1033 cm^{-1}, related to the stretching of the acetal groups C-O-C-O-C found in the structure of cellulose and hemicellulose, becomes more intense when compared to the other purification methods. This could be due to the overlapping of the asymmetric stretching vibration of Si-O-Si present in amorphous silica, which exhibits a characteristic band at 1100 cm^{-1} (Do et al., 2020; Le et al., 2015). The typical stretching vibration of the β-glycosidic bond (C-O-C) present in the cellulose appeared at 898 cm^{-1} becoming more defined and intense as the purification process progressed.

Fig. 4b shows the XRD patterns and crystallinity index (*CI*) of the untreated RS and the fractions obtained with the different purification treatments before and after the bleaching step. All of the samples showed the same typical crystalline profile of cellulose Iβ, with diffraction peaks at $2\theta = 15°$ ($1\bar{1}0$), 16° (110), 22° (200), and 34° (004) (Chen et al., 2011; Freitas et al., 2022a, 2022b). The maintenance of the most abundant allomorphic form of cellulose found in nature suggested that none of the treatments tested, even the alkaline, altered its crystalline arrangement (Nam et al., 2016). In general, the diffraction peaks were sharper (mainly the one corresponding to (200)) and CI increased after the bleaching treatment, coherently with the elimination of amorphous components, including hemicellulose, lignin, waxes, and

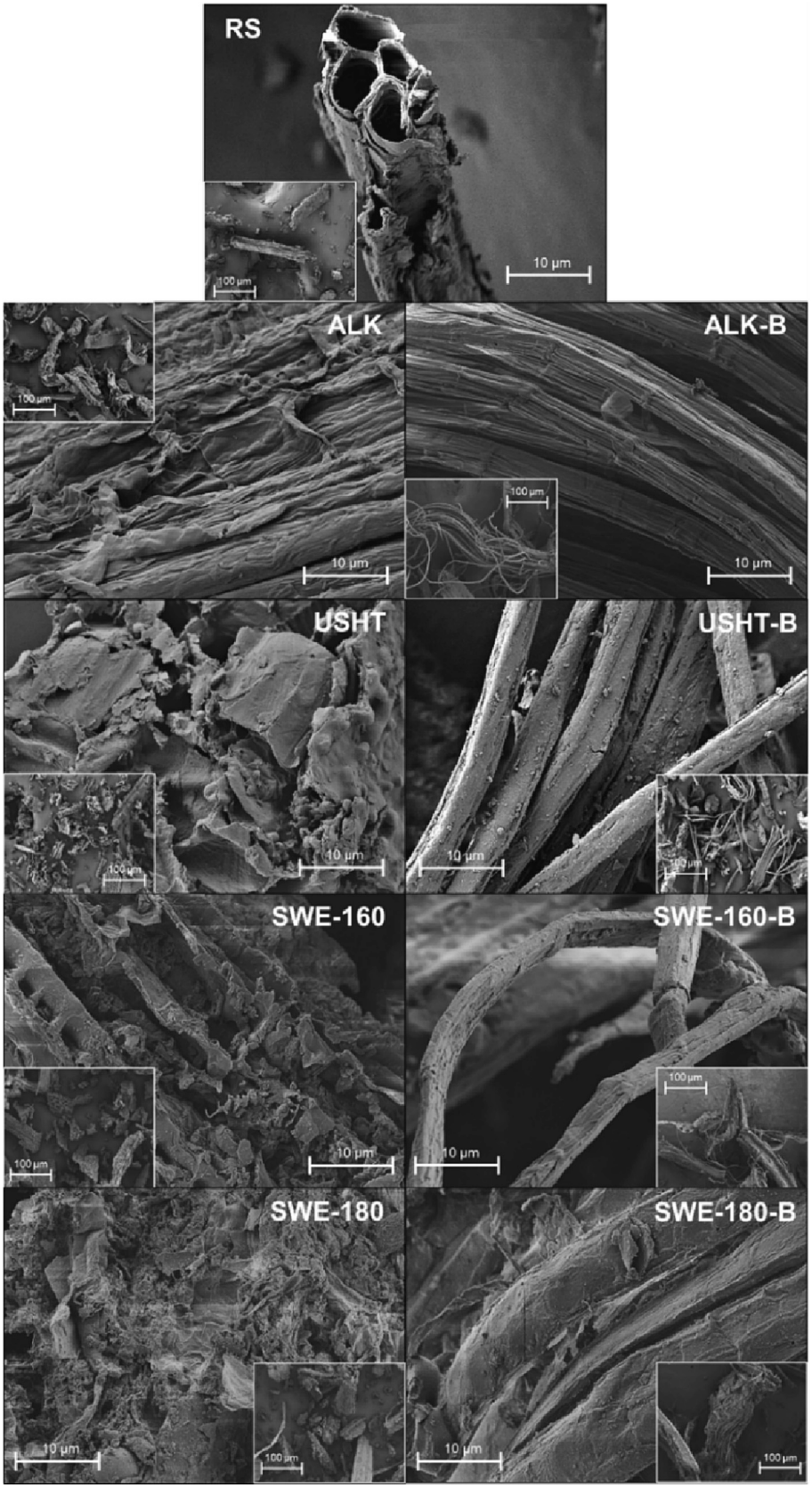

Fig. 2. FESEM micrographs of the raw RS and the different lignocellulosic fractions obtained before and after the bleaching step.

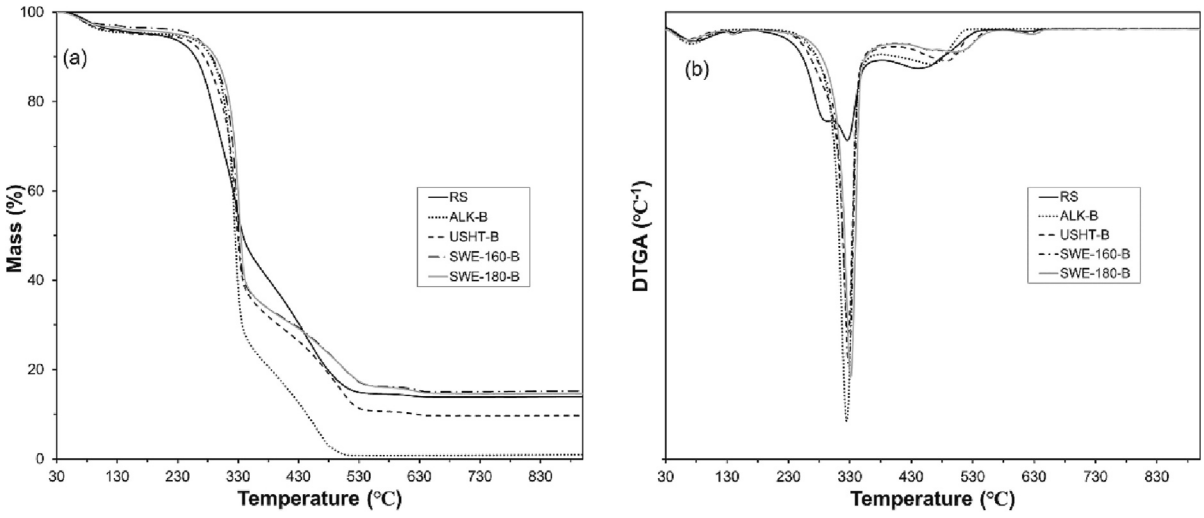

Fig. 3. TGA and DTGA curves of the raw RS samples and cellulosic fractions obtained with the different purification methods after the bleaching step.

Table 3
Onset (T_{on}) and peak (T_p) temperatures and mass loss (%Δm) of the different thermodegradation steps and final residual mass of cellulosic materials obtained with different purification pre-treatments (mean values ± standard deviation of two replicates).

Treatment	[40–180] °C			[160–400] °C			[380–660] °C			Residue (%)
	T_{on}*	T_p*	Δm (%)	T_{on}*	T_p*	Δm (%)	T_{on}*	T_p*	Δm (%)	
RS	39 ± 1^{b}	79 ± 7^{ab}	5 ± 1^{a}	171 ± 7^{cd}	327 ± 1^{b}	57 ± 1^{d}	391 ± 9^{ab}	446 ± 4^{cd}	13 ± 1^{ab}	17 ± 2^{a}
ALK	44 ± 1^{a}	66 ± 5^{c}	5 ± 1^{a}	179 ± 1^{c}	301 ± 3^{c}	57 ± 3^{cd}	372 ± 1^{c}	427 ± 11^{e}	25 ± 4^{ab}	8 ± 1^{bc}
USHT	38 ± 1^{b}	81 ± 5^{a}	5 ± 2^{a}	178 ± 1^{c}	323 ± 4^{b}	62 ± 1^{bc}	379 ± 6^{bc}	444 ± 4^{de}	26 ± 2^{a}	10 ± 2^{b}
SWE-160	45 ± 1^{a}	72 ± 5^{abc}	5 ± 1^{a}	170 ± 1^{cd}	322 ± 4^{b}	54 ± 2^{d}	387 ± 5^{b}	461 ± 3^{c}	25 ± 1^{ab}	15 ± 1^{a}
SWE-180	43 ± 2^{a}	70 ± 4^{bc}	4 ± 2^{a}	167 ± 6^{d}	327 ± 2^{ab}	56 ± 3^{d}	392 ± 4^{ab}	460 ± 2^{cd}	27 ± 1^{a}	13 ± 5^{ab}
ALK-B	41 ± 1^{ab}	70 ± 5^{c}	4 ± 2^{a}	203 ± 6^{a}	324 ± 1^{b}	73 ± 1^{a}	368 ± 6^{c}	477 ± 11^{b}	22 ± 2^{bc}	2 ± 3^{cd}
USHT-B	43 ± 3^{ab}	73 ± 2^{abc}	4 ± 1^{a}	192 ± 6^{b}	327 ± 1^{ab}	66 ± 1^{b}	401 ± 1^{a}	495 ± 11^{a}	19 ± 1^{cd}	7 ± 2^{bc}
SWE-160-B	45 ± 1^{a}	66 ± 2^{c}	4 ± 1^{a}	196 ± 1^{ab}	327 ± 1^{ab}	64 ± 1^{b}	393 ± 10^{ab}	504 ± 6^{a}	16 ± 1^{d}	15 ± 1^{a}
SWE-180-B	42 ± 4^{ab}	70 ± 4^{bc}	4 ± 2^{a}	192 ± 3^{b}	331 ± 1^{a}	64 ± 2^{b}	401 ± 1^{a}	501 ± 1^{a}	16 ± 2^{d}	15 ± 3^{a}

Different subscript letters in the same column indicate significant differences by the Tukey test ($p < 0.05$).

silica, thereby realigning the cellulose chains (Li et al., 2009; Zainuddin et al., 2013). Fibres obtained with the alkaline treatment exhibited the greatest CI values before and after the bleaching process (62 and 69 %, respectively) whereas the USHT treatment produced the fibres with the lowest *CI* (45 and 60 %, respectively, before and after bleaching), probably due to the fact that they had the highest content in amorphous hemicellulose (Table 2). On the other hand, a slight shift of the peak corresponding to the plane (200) was observed for the ALK samples, before and after bleaching. This behaviour could be explained by the rearrangement of cellulose chains caused by the penetration of Na^{+} ions in the crystalline network to form antiparallel crystalline soda-cellulose complexes, as described by Budtova and Navard (2016), Liu and Hu (2008), and Freitas et al. (2022a, 2022b).

3.1.5. *Hydrogel formation capacity*

The ability of the different bleached CFs to form hydrogels through cyclic freezing-thawing (FT) was evaluated. Fig. 5 shows the aqueous suspensions of different CFs obtained after the sonication step and their changes after each FT cycle.

All of the fibres gave rise to homogeneous and viscous suspensions, indicating that the sonication step was effective at both defibrillating the CF bundles and dispersion. However, marked differences were observed between the hydrogels produced with the different CFs. The hydrogel from the USHT-B fibres showed the best physical integrity, with a similar appearance after the three FT cycles. A slight degree of hydrogel compaction and syneresis was observed after each FT cycle, due to the progressive association of the CFs, which provoked the decrease in the water holding capacity of the CF three-dimensional network (Jiang & Hsieh, 2014). These changes were more noticeable for the hydrogels obtained by treatments other than USHT-B, with a slight increase in visual compactness and syneresis for the ALK-B hydrogel, followed by SWE-160-B hydrogel. The SWE-180-B fibre produced much weaker hydrogels with a low water holding capacity, even after the first FT cycle. As reported by Abdel-Mohsen et al. (2011) and Figueroa-Pizano et al. (2020), three-dimensional network arrangements of hydrogels, obtained by the FT method, are markedly influenced by the freezing temperature and the rate, time and number of FT cycles, the nature of the polymer, and the polymer: solvent ratio. The formation of hydrogels via the FT method is due to the cryoconcentration of the water solution containing the polymers during water crystallisation, which provokes the association of the polymer chains to form polymeric domains surrounding the nuclei of ice crystals, thus becoming hydrogels when the system thaws (Abdel-Mohsen et al., 2011; Jiang & Hsieh, 2014). The type and concentration of polymers influence the strength and degree of interaction between their chains under each FT condition, granting physical integrity for the three-dimensional polymer network. The differences between the gelling capacity observed in the samples could be related to their different composition. The hemicellulose content of CFs could play an important role in the hydrogel structure due to its greater water solubility. There was a greater amount of hemicellulose in the USHT-B fibres, followed by ALK—B, SWE-160-B, and SWE-180-B. So, this could favour the polymer association, together with the cellulose fibrils, thus contributing to the formation of a more cohesive hydrogel structure. In fact, in the SWE-180-B hydrogel with the lowest content of hemicellulose (~3 %), an inhomogeneous hydrogel with a poor water holding capacity was obtained. Likewise, in the case of the hydrogels

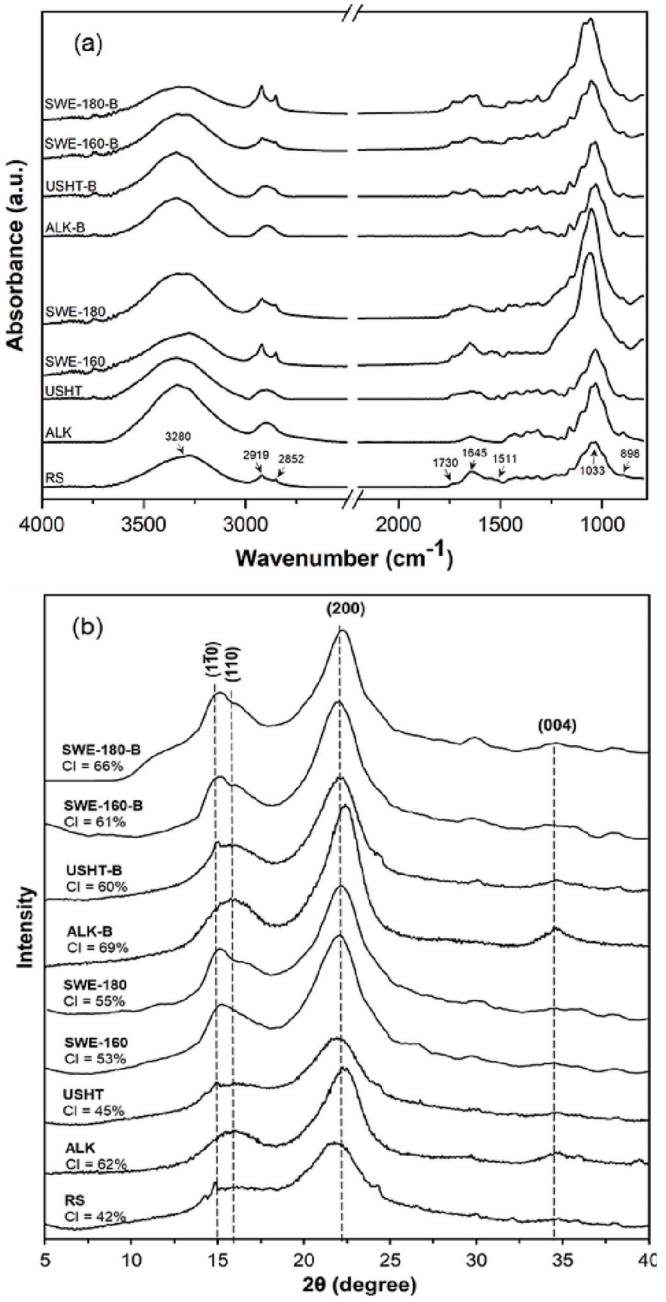

Fig. 4. FTIR (a) and XRD (b) spectra of the untreated RS and the cellulosic fractions purified by different treatments before and after the bleaching step.

with intermediate hemicellulose contents (~10 % in the ALK-B and SWE-160-B samples), they also exhibited intermediate visual firmness and water holding capacity. Nevertheless, the presence of silica could also affect the hydrogel formation, since, with similar hemicellulose contents, ALK-B hydrogels presented a more cohesive structure than the silica-rich SWE-160-B hydrogels, at every FT cycle. This could be attributed to the hydrogen bond formation between silica particles and hydroxyl groups of polymers that interfere with the polymer association in the cryoconcentrated domains. Hydrogen bonds of amorphous silica particles and hydroxyl groups have been observed by Cabrera et al. (2016) through the use of NMR and FTIR techniques.

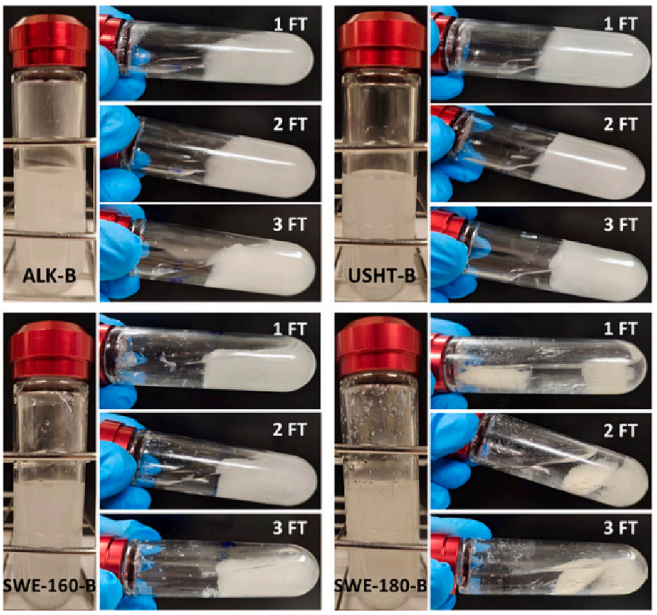

Fig. 5. Photographs of the sonicated bleached CF suspensions (vertical tubes) and their respective hydrogels (horizontal tubes) after each freezing-thawing (FT) cycle.

3.2. *Properties of aerogels*

3.2.1. *Appearance and microstructure*

Fig. 6 shows the visual appearance and FESEM micrographs of aerogels prepared with the different bleached CFs. Observation with the naked eye showed unnoticeable differences between the ALK-B and USHT-B aerogels, which exhibited a cohesive spongy structure with a smooth surface. A more fibrillar arrangement and a rough surface were observed for the aerogels obtained from SWE fibres, which was more marked for the SWE-180-B sample.

FESEM micrographs revealed no marked structural differences between the ALK—B, USHT-B, and SWE-160-B aerogels, which showed irregularly dispersed micrometric pores, with film-like lamellas surrounding the cellulose fibres. The formation of these lamellas could be attributed to the presence of hemicellulose and other water-soluble compounds, which were aggregated during the cryoconcentration of the water fibre dispersions, in line with the ice crystal formation, wrapping the cellulose fibres and generating the interconnected lamellas in the freeze-dried material. Aerogels obtained with the SWE-180-B CFs with very low hemicellulose content, exhibited a more filamentous structure with a less evident interconnecting lamellar structure.

The pore sizes in the aerogels depend on the ice crystal growth that occurred during the freezing step. This is affected by the sample cooling rate that determines the nucleation rate and nuclei propagation, which is greatly affected by the solution viscosity and molecular diffusion (Jiang & Hsieh, 2014). Soluble hemicellulose may increase the solution viscosity, thus affecting the final crystal size and consequently the pore sizes in the aerogel after the ice sublimation. Jiang and Hsieh (2014) observed changes in the aerogel pore sizes and wall thickness depending on the rate of ice formation in RS cellulose nanocrystal suspensions. The higher the cooling rate, the greater the number of nuclei formed and the smaller the crystal sizes, which gave rise to smaller pores in the aerogel structure. Likewise, as ice crystals grow more slowly and larger, more solids are cryo-concentrated to assemble into ordered domains around larger crystals resulting in thicker walls in the aerogel. The poorer physical integrity of the aerogels from SWE-180-B fibres, as also observed in the corresponding hydrogel, could be related with the lower ratio of soluble polymer, such as hemicellulose, which contributes to the wall formation. Mandin et al. (2021) obtained cellulose nanofibre

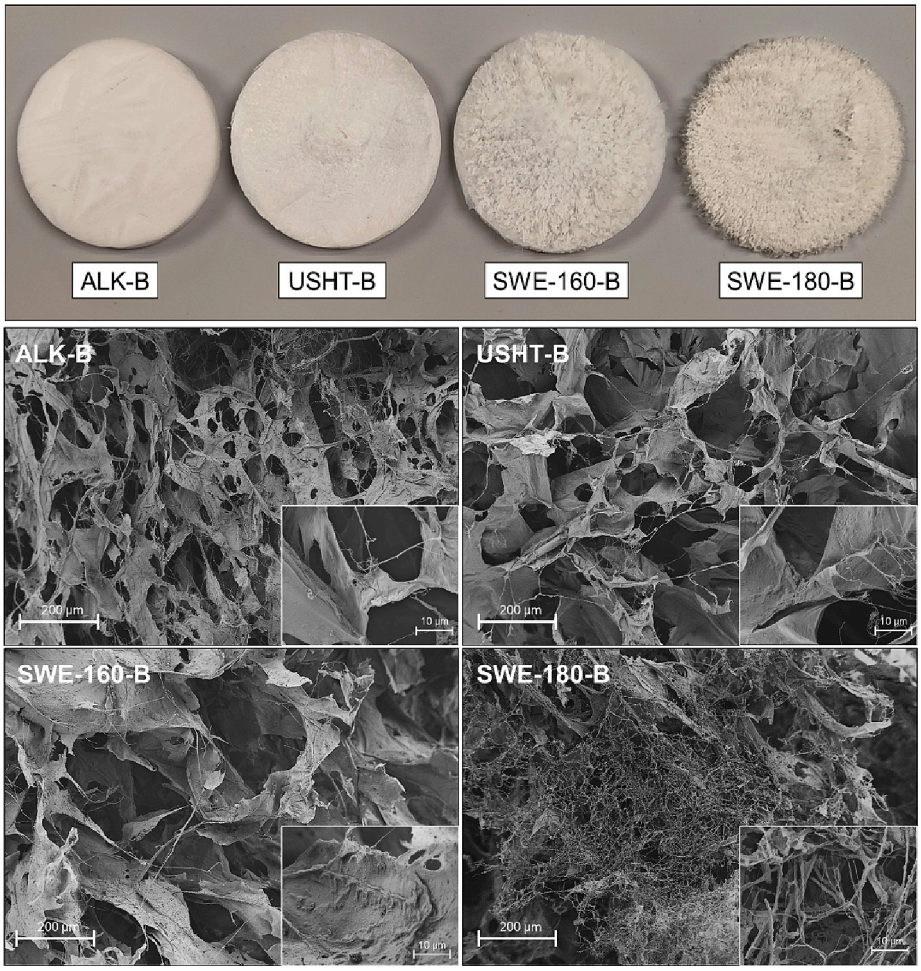

Fig. 6. Visual appearance and FESEM micrographs (x100 magnification with embedded micrographs at x2000 magnification) of cellulose aerogels prepared with bleached CF obtained via different purification processes: alkaline treatment, combined ultrasound-reflux heating, and subcritical water extraction at 160 °C and 180 °C.

aerogels with and without xyloglucan, a hemicellulose fraction extracted from tamarind seed, and found structural differences associated with the presence of xyloglucan.

On the other hand, as previously observed for the hydrogels, the presence of a high silica ratio could also affect the aerogel microstructure. Hydrogen bonds between silanediol and silanol forms of silica (Mochidzuki et al., 2001) and polymers or fibres could affect the interchain forces in the solid domains, thus contributing to modify the cohesion forces in the aerogel three-dimensional network. Thus, both SWE-160-B and SWE-180-B silica-rich aerogels exhibited poorer physical integrity which could be, in part, attributed to the silica interactions with the chemical groups present in the cellulose and hemicellulose chains (Cabrera et al., 2016; Do et al., 2020; Le et al., 2015).

3.2.2. *Water sorption isotherms*

All of the cellulose aerogels exhibited type II isotherms, with a prevalent monolayer adsorption of water molecules at low water activity (a_w) and subsequent multilayer adsorption at intermediate a_w values. There was no water capillary condensation in the pores in the studied range, since this phenomenon would occur at higher water activity ($a_w > 0.95$) (Aviara, 2020). The experimental data were modelled by fitting the GAB equation, which is applicable over a wide range of a_w values (Baptestini et al., 2020). Fig. 7 shows the experimental points and the GAB fitted model ($R^2 > 0.91$) for the different aerogels, as well as the GAB parameters (embedded table in the figure). The water sorption levels at each a_w value was in the range of what has previously been reported for fibres from different cellulosic derivatives, with sorption properties correlated to the accessibility and the amount of sorption sites and also to the degree of crystallinity of the fibres (Simon et al., 2022). The differences in the water sorption behaviour of the different materials over the studied a_w range must be attributed to compositional differences (Table 2) and degree of crystallinity (Fig. 4). The samples from the USHT treatment exhibited a greater moisture sorption capacity, which could be attributed to the higher content of amorphous hemicellulose and the lower level of crystallinity of the material (60 %), which promotes water binding capacity, as previously described (Ioelovich & Leykin, 2010). In contrast, samples from the ALK treatment with a higher cellulose content and greater crystallinity exhibited a lower water binding capacity. Nevertheless, the high silica content in samples from the SWE treatments could also interfere with the water sorption behaviour of the material due to the above commented interactions of silanediol and silanol forms of silica with the cellulose hydroxyl groups that make them unavailable for water molecules, reducing the water binding capacity of the material. Hydrogen bonds of amorphous silica particles with hydroxyl groups have been demonstrated through NMR and FTIR analyses (Cabrera et al., 2016). In fact, the SWE-180-B sample, with a high degree of crystallinity (66 %) and a high silica content (15 %), exhibited the lowest water sorption capacity within the a_w range.

The monolayer moisture contents of the different samples were also obtained from the experimental data by fitting the BET model (for $a_w < 0.4$) and the specific surface area (SSA) of each aerogel sample was

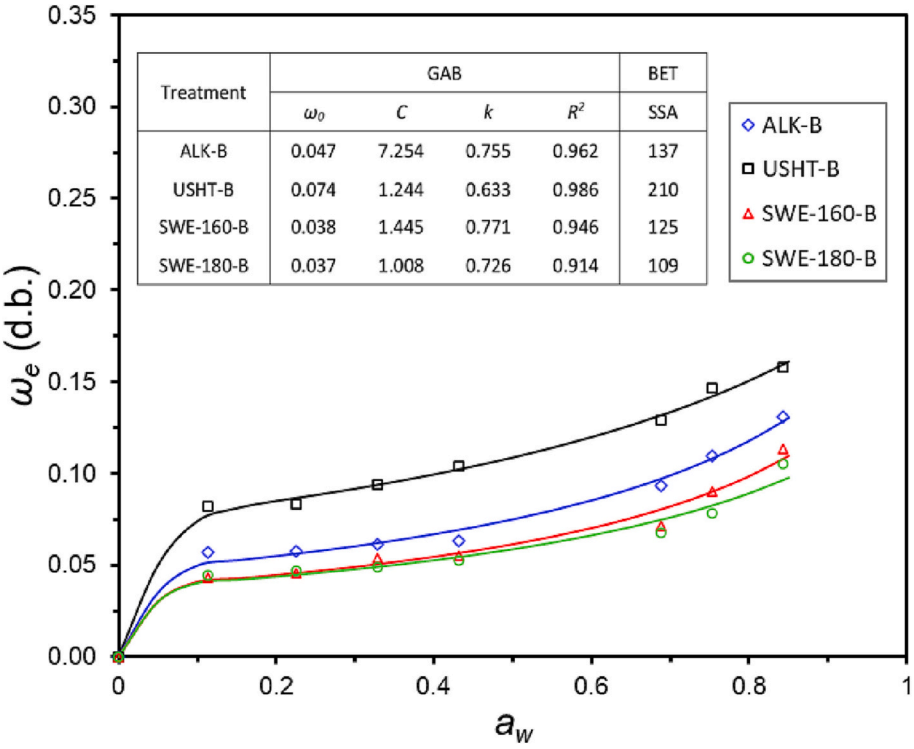

Fig. 7. Sorption isotherms of the cellulosic aerogels obtained from the cellulose fractions purified by the different treatments. The experimental points, the fitted GAB model (lines), and the parameters of the fitted GAB model obtained for the different aerogels (inserted table). The values of specific surface area (SSA) values ($m^2.g^{-1}$) obtained from BET analyses of sorption data for $a_w < 0.4$ were also included.

determined by considering the area of the water molecule on the adsorbent substrate (inserted table in Fig. 7). These values were between 109 and 201 $m^2.g^{-1}$ for the different samples, within the range of aerogel materials. As expected, the SSA values of the samples were correlated with the water binding capacity of the different materials.

3.2.3. *Porosity and water absorption and retention capacities of aerogels*

The effects of the purification treatments of CFs on the properties of cellulose aerogels were also evaluated in terms of density, porosity, water absorption, and water retention capacity (Table 4). Very low density (5.3–6.1 $mg.cm^{-3}$) and high porosity (98.8–99.1 %) values were observed for ALK—B, USHT-B, and SWE-160-B aerogels, typical of ultralightweight and porous materials. These values are comparable to graphene and silica aerogels, which exhibited density and porosity values of about 4 $mg.cm^{-3}$ and 98.2 % (Ngoc Hong, 2017; Xie et al., 2016), and 70–150 $mg.cm^{-3}$ and 80–93 % (Amirjan et al., 2012; Buratti & Moretti, 2013), respectively. Nonetheless, the SWE-180-B aerogel exhibited higher density (16.8 $mg.cm^{-3}$) and significantly ($p < 0.05$) lower porosity (96.7 %), in coherence with the marked structural differences observed by the FESEM analysis, where more filamentous and less interconnecting lamellar structure was observed. This could imply higher gravitational collapse of the network producing denser aerogels. The measured porosity values were always lower than the theoretical, since the film density was lower than the theoretical density value of crystalline cellulose (1600 $mg.cm^{-3}$, Diddens et al., 2008). This means that the fibre packing in the films was more open than in crystalline cellulose, including non-removed compounds and bonded water, which reduces the real density of the cellulosic material. Likewise, the density of cellulose films was greatly affected by the previous purification and homogenisation method due to the presence of empty spaces or pores among the fibrils (Spence et al., 2010). The samples richer in silica (SWE-160-B and SWE-180-B) exhibited lower film density, which points to the contribution of this compound to the fibre arrangement in the films, forming a less compact, lighter structure, despite the higher density of silica.

Table 4
Density, porosity, water sorption, and water retention capacity values of the different cellulose aerogels. Mean values and standard deviation.

	ALK-B	USHT-B	SWE-160-B	SWE-180-B
Density ($mg.cm^{-3}$)	6.1 ± 0.7^{b}	5.5 ± 0.3^{b}	5.3 ± 0.1^{b}	16.8 ± 1.6^{a}
Measured porosity (%)	98.9 ± 0.1^{ab}	99.1 ± 0.1^{a}	98.8 ± 0.1^{b}	96.7 ± 0.4^{c}
Theoretical porosity (%)	99.6 ± 0.1^{a}	99.7 ± 0.2^{a}	99.7 ± 0.1^{a}	98.9 ± 0.1^{b}
Film density ($mg.cm^{-3}$)	554 ± 63^{a}	587 ± 26^{a}	463 ± 7^{b}	435 ± 5^{c}
Theoretical WAC ($g.g^{-1}$ aerogel)	182 ± 11^{a}	183 ± 11^{a}	188 ± 5^{a}	59 ± 5^{b}
Measured WAC ($g.g^{-1}$ aerogel)	55.6 ± 1.6^{a}	52.3 ± 2.9^{ab}	45 ± 4^{b}	49 ± 4^{ab}
WRC ($g.g^{-1}$ aerogel)	1.0 ± 0.3^{a}	0.2 ± 0.1^{c}	0.2 ± 0.1^{bc}	0.5 ± 0.2^{b}

WAC: water absorption capacity; WRC: water retention capacity. Different subscript letters in the same line indicate significant differences by means of the Tukey test ($p < 0.05$).

All of the aerogels exhibited high water absorption capacities (WAC values), ranging from 49 to 56 g $water.g^{-1}$ aerogel. These WAC values are within the range found for different nanocellulose aerogels (Alakalhunmaa et al., 2016; Mandin et al., 2021; Yang & Cranston, 2014; W. Zhang et al., 2012) when crosslinking agents were not added. Using crosslinkers, such as polyamide-epichlorohydrin resin, water absorption capacity of cellulose aerogeles was highly promoted due to the strong inter-fibre interactions after chemical crosslinking (Zhang et al., 2012). The theoretical WAC, determined from the porosity values, was higher in every sample than the determined WAC. This is explained by the partial collapse of the aerogel structure when it swells in contact with water, which leads to a loss in water absorption capacity with respect to that predicted from the air volume. The SWE-180-B aerogel exhibited

the smallest difference between the real and theoretical WAC values, thus indicating that its structure collapses less during the wetting process. The structural collapse is related with the water interactions with the aerogel structure and its ability to dissolve components relevant in the three-dimensional building of aerogel. The macroscopic integrity of cellulose aerogels is maintained through hydrogen bonding and entanglements between adjacent nano or microfibrils. Therefore, when immersed in water, the cellulose-cellulose hydrogen bonds can be replaced by cellulose-water hydrogen bonds and the network structure of the aerogel can be fully destroyed. In this sense, covalent crosslinking (Zhang et al., 2012) or coating with hydrophobic polymers (Benito-González et al., 2020) have been described to improve water-resistance of aerogel. The different hydration collapse of the aerogel samples suggests that the stablished hydrogen bonds responsible for the aerogel structure could be divided in two categories: those replaced by water bonds during water immersion and those resistant to water replacement that remain in the sample structure and are responsible for water absorption and retention capacities. In SWE-180-B aerogels, the second bond category are mainly present, as compared to the other aerogels, where a higher ratio of structural hydrogen bonds was broken during hydration, inducing higher collapse.

As concerns the water retention capacity (WRC), the ALK-B aerogel exhibited the highest WRC value ($p < 0.05$), followed by the SWE-180-B samples, while the other treatments exhibited similar values ($p > 0.05$). The higher WRC of ALK-B could be related to its higher proportion of cellulose and lower hemicellulose content, which may promote the structural strength of the aerogel and resistance to the hydration collapse. In fact, this sample exhibited the highest WAC and higher water retention by capillary forces and extensive hydrogen bonds could be expected if more pores remained available after hydration. Fontes-Candia et al. (2019) found similar levels of water retention by aerogels produced from *Arundo donax* sugarcane biomass.

4. Conclusions

The USHT and SWE alternative extraction methods were effective at eliminating non-cellulosic compounds, but to a different degree compared to the commonly-used ALK treatment. The SWE treatment at 180 °C was more effective at eliminating hemicelluloses, while the ALK and USHT methods gave rise to fibres richer in hemicellulose with the lowest silica content.

The final composition of the bleached CFs markedly affected the structure and properties of the cellulose-based hydrogels and aerogel obtained. Thus, a higher hemicellulose content in the CF led to more consistent hydrogels with a greater water holding capacity and to aerogels with thicker walls and higher porosity and water vapour sorption capacity. In contrast, the presence of silica gave rise to weaker hydrogels and fibrous aerogels, with lower porosity and poorer water absorption capacity.

Therefore, RS can be valorised to obtain high added value cellulosic materials, such as aerogels, using aqueous extraction, by applying ultrasounds or subcritical conditions to favour cellulosic purification. The different extraction methods can offer materials of specific composition and therefore targeted properties.

CRediT authorship contribution statement

Pedro A.V. Freitas: Conceptualization, Methodology, Formal analysis, Investigation, Writing – original draft, Writing – review & editing. **Consuelo González-Martínez:** Conceptualization, Methodology, Formal analysis, Investigation, Writing – original draft, Writing – review & editing. **Amparo Chiralt:** Conceptualization, Methodology, Formal analysis, Investigation, Writing – original draft, Writing – review & editing.

Declaration of competing interest

The authors declare that they have no known competing financial interests or personal relationships that could have appeared to influence the work reported in this paper.

Data availability

Data will be made available on request.

Acknowledgments

The authors thank the Agencia Estatal de Investigación (Spain) for the financial support through project PID2019-105207RB-I00/AEI/10.13039/501100011033 and Generalitat Valenciana for funding the project CIPROM/2021/071 and grant GrisoliaP/2019/115.

References

Abdel-Mohsen, A. M., Aly, A. S., Hrdina, R., Montaser, A. S., & Hebeish, A. (2011). Eco-synthesis of PVA/chitosan hydrogels for biomedical application. *Journal of Polymers and the Environment, 19*(4), 1005–1012. https://doi.org/10.1007/s10924-011-0334-0

Abd-Talib, N., Mohd-Setapar, S. H., Asli, U. A., Pa'ee, K. F., Len, K. Y. T., & Mohd-Nasir, H. (2020). Silica removal by alkaline hydrogen peroxide treatment to enhance the conversion of rice straw to sugars. *Materials Today: Proceedings, 31*, 145–149. https://doi.org/10.1016/j.matpr.2020.01.397

Abe, K., & Yano, H. (2009). Comparison of the characteristics of cellulose microfibril aggregates of wood, rice straw, and potato tuber. *Cellulose, 16*, 1017–1023. https://doi.org/10.1007/s10570-009-9334-9

Alakalhunmaa, S., Parikka, K., Penttilä, P. A., Cuberes, M. T., Willför, S., Salmén, L., & Mikkonen, K. S. (2016). Softwood-based sponge gels. *Cellulose, 23*(5), 3221–3238. https://doi.org/10.1007/s10570-016-1010-2

Amirjan, E., Mirzaee, O., Soleimani Dorcheh, M. R., & Dorcheh, A. S. (2012). Preparation and characterization of nanoporous silica aerogel granules on the basis of water glass via ambient pressure drying method. *Jurnal Teknologi, 59*(2). https://doi.org/10.11113/jt.v59.2598

Aviara, N. (2020). Moisture sorption isotherms and isotherm model performance evaluation for food and agricultural products. In G. Kyzas, & N. Lazaridis (Eds.), *Sorption in 2020s*. IntechOpen. https://doi.org/10.5772/intechopen.87996.

Baptestini, F. M., Corrêa, P. C., Ramos, A. M., Junqueira, M.d. S., & Zaidan, I. R. (2020). GAB model and the thermodynamic properties of moisture sorption in soursop fruit powder. *Revista Ciência Agronômica, 51*(1). https://doi.org/10.5935/1806-6690.20200006

Barana, D., Salanti, A., Orlandi, M., Ali, D. S., & Zoia, L. (2016). Biorefinery process for the simultaneous recovery of lignin, hemicelluloses, cellulose nanocrystals and silica from rice husk and Arundo donax. *Industrial Crops and Products, 86*, 31–39. https://doi.org/10.1016/j.indcrop.2016.03.029

Benito-González, I., López-Rubio, A., Gómez-Mascaraque, L. G., & Martínez-Sanz, M. (2020). PLA coating improves the performance of renewable adsorbent pads based on cellulosic aerogels from aquatic waste biomass. *Chemical Engineering Journal, 390*, Article 124607. https://doi.org/10.1016/j.cej.2020.124607

Bochek, A. M. (2003). Effect of hydrogen bonding on cellulose solubility in aqueous and nonaqueous solvents. *Russian Journal of Applied Chemistry, 76*(11), 1711–1719. https://doi.org/10.1023/B:RJAC.0000018669.88546.56

Budtova, T. (2019). Cellulose II aerogels: A review. *Cellulose, 26*, 81–121. https://doi.org/10.1007/s10570-018-2189-1

Budtova, T., & Navard, P. (2016). Cellulose in NaOH-water based solvents: A review. *Cellulose, 23*(1). https://doi.org/10.1007/s10570-015-0779-8

Buratti, C., & Moretti, E. (2013). Silica nanogel for energy-efficient windows. In *Nanotechnology in eco-efficient construction* (pp. 207–235). https://doi.org/10.1533/9780857098832.2.207

Cabrera, Y., Cabrera, A., Larsen, F. H., & Felby, C. (2016). Solid-state 29Si NMR and FTIR analyses of lignin-silica coprecipitates. *Holzforschung, 70*(8), 709–718. https://doi.org/10.1515/hf-2015-0165

Castro-Puyana, M., Herrero, M., Mendiola, J. A., & Ibáñez, E. (2013). Subcritical water extraction of bioactive components from algae. In *Functional ingredients from algae for foods and nutraceuticals* (pp. 534–560). Elsevier. https://doi.org/10.1533/9780857098689.3.534.

Chen, X., Yu, J., Zhang, Z., & Lu, C. (2011). Study on structure and thermal stability properties of cellulose fibers from rice straw. *Carbohydrate Polymers, 85*(1), 245–250. https://doi.org/10.1016/j.carbpol.2011.02.022

Collazo-Bigliardi, S., Ortega-Toro, R., & Chiralt Boix, A. (2018). Isolation and characterisation of microcrystalline cellulose and cellulose nanocrystals from coffee husk and comparative study with rice husk. *Carbohydrate Polymers, 11*. https://doi.org/10.1016/j.carbpol.2018.03.022

Collazo-Bigliardi, S., Ortega-Toro, R., & Chiralt Boix, A. (2018). Reinforcement of thermoplastic starch films with cellulose fibres obtained from rice and coffee husks. *Journal of Renewable Materials, 6*(7), 599–610. https://doi.org/10.32604/JRM.2018.00127

Diddens, I., Murphy, B., Krisch, M., & Müller, M. (2008). Anisotropic elastic properties of cellulose measured using inelastic X-ray scattering. *Macromolecules, 41*, 9755–9759. https://doi.org/10.1021/ma801796u

Do, N. H., Pham, H. H., Le, T. M., Lauwaert, J., Diels, L., Verberckmoes, A., Do, N. H. N., Tran, V. T., & Le, P. K. (2020). The novel method to reduce the silica content in lignin recovered from black liquor originating from rice straw. *Scientific Reports, 10* (1), 21263. https://doi.org/10.1038/s41598-020-77867-5

El-Sakhawy, M., & Hassan, M. L. (2007). Physical and mechanical properties of microcrystalline cellulose prepared from agricultural residues. *Carbohydrate Polymers, 10*. https://doi.org/10.1016/j.carbpol.2006.04.009

Esteves, B., Velez Marques, A., Domingos, I., & Pereira, H. (2013). Chemical changes of heat treated pine and eucalypt wood monitored by FTIR. *Maderas. Ciencia y Tecnología*, 245–258. https://doi.org/10.4067/S0718-221X2013005000020

Ferreira, E. S., Rezende, C. A., & Cranston, E. D. (2021). Fundamentals of cellulose lightweight materials: Bio-based assemblies with tailored properties. *Green Chemistry, 23*(10), 3542–3568. https://doi.org/10.1039/D1GC00326G

Figueroa-Pizano, M. D., Vélaz, I., & Martínez-Barbosa, M. E. (2020). A freeze-thawing method to prepare chitosan-poly(vinyl alcohol) hydrogels without crosslinking agents and diflunisal release studies. *Journal of Visualized Experiments, 155*, 59636. https://doi.org/10.3791/59636

Fontes-Candia, C., Erboz, E., Martínez-Abad, A., López-Rubio, A., & Martínez-Sanz, M. (2019). Superabsorbent food packaging bioactive cellulose-based aerogels from Arundo donax waste biomass. *Food Hydrocolloids, 96*, 151–160. https://doi.org/10.1016/j.foodhyd.2019.05.011

Freitas, P. A. V. (2023). *Valorisation of rice straw by obtaining active compounds and cellulosic materials for the development of biodegradable food packaging systems.* Universitat Politècnica de València. Doctoral dissertation.

Freitas, P. A. V., Arias, C. I. L. F., Torres-Giner, S., González-Martínez, C., & Chiralt, A. (2021). Valorization of rice straw into cellulose microfibers for the reinforcement of thermoplastic corn starch films. *Applied Sciences, 11*(18), 8433. https://doi.org/10.3390/app11188433

Freitas, P. A. V., Gil, N. J. B., González-Martínez, C., & Chiralt, A. (2022). Antioxidant poly (lactic acid) films with rice straw extract for food 2 packaging applications. *Food Packaging and Shelf Life, 30*. https://doi.org/10.1016/j.fpsl.2022.101003

Freitas, P. A. V., González-Martínez, C., & Chiralt, A. (2020). Application of ultrasound pre-treatment for enhancing extraction of bioactive compounds from rice straw. *Foods, 9*(11), 1657. https://doi.org/10.3390/foods9111657

Freitas, P. A. V., González-Martínez, C., & Chiralt, A. (2022). Applying ultrasound-assisted processing to obtain cellulose fibres from rice straw to be used as reinforcing agents. *Innovative Food Science & Emerging Technologies, 76*, Article 102932. https://doi.org/10.1016/j.ifset.2022.102932

Habibi, Y., Lucia, L. A., & Rojas, O. J. (2010). Cellulose nanocrystals: Chemistry, self-assembly, and applications. *Chemical Reviews, 110*(6). https://doi.org/10.1021/cr900339w

Henschen, J., Illergård, J., Larsson, P. A., Ek, M., & Wågberg, L. (2016). Contact-active antibacterial aerogels from cellulose nanofibrils. *Colloids and Surfaces B: Biointerfaces, 146*, 415–422. https://doi.org/10.1016/j.colsurfb.2016.06.031

Ioelovich, M., & Leykin, A. (2010). Study of sorption properties of cellulose and its derivatives. *BioResources, 6*(1), 178–195. https://doi.org/10.15376/biores.6.1.178-195

Jiang, F., Han, S., & Hsieh, Y.-L. (2013). Controlled defibrillation of rice straw cellulose and self-assembly of cellulose nanofibrils into highly crystalline fibrous materials. *RSC Advances, 3*(30), 12366. https://doi.org/10.1039/c3ra41646a

Jiang, F., & Hsieh, Y.-L. (2014). Super water absorbing and shape memory nanocellulose aerogels from TEMPO-oxidized cellulose nanofibrils via cyclic freezing–thawing. *Journal of Materials Chemistry A, 2*(2), 350–359. https://doi.org/10.1039/C3TA13629A

Kistler, S. S. (1932). Coherent expanded aerogels. *The Journal of Physical Chemistry, 36*, 52–64. https://doi.org/10.1038/127741a0

Le, D. M., Sørensen, H. R., Knudsen, N. O., & Meyer, A. S. (2015). Implications of silica on biorefineries—Interactions with organic material and mineral elements in grasses. *Biofuels, Bioproducts and Biorefining, 9*(1), 109–121. https://doi.org/10.1002/bbb.1511

Li, R., Fei, J., Cai, Y., Li, Y., Feng, J., & Yao, J. (2009). Cellulose whiskers extracted from mulberry: A novel biomass production. *Carbohydrate Polymers, 76*(1), 94–99. https://doi.org/10.1016/j.carbpol.2008.09.034

Liu, Y., & Hu, H. (2008). X-ray diffraction study of bamboo fibers treated with NaOH. *Fibers and Polymers, 9*(6), 735–739. https://doi.org/10.1007/s12221-008-0115-0

Long, L.-Y., Weng, Y.-X., & Wang, Y.-Z. (2018). Cellulose aerogels: Synthesis, applications, and prospects. *Polymers, 10*(6), 623. https://doi.org/10.3390/polym10060623

Mandin, S., Moreau, S., Talantikite, M., Novalès, B., Maigret, J.-E., Cathala, B., & Moreau, C. (2021). Cellulose nanofibrils/xyloglucan bio-based aerogels with shape recovery. *Gels, 7*(1), 5. https://doi.org/10.3390/gels7010005

Mansaray, G., & Ghaly, A. E. (1998). Thermal degradation of rice husks in nitrogen atmosphere. *Bioresource Technology, 65*, 13–20. https://doi.org/10.1016/S0960-8524(98)00031-5

Mochidzuki, K., Sakoda, A., Suzuki, M., Izumi, J., & Tomonaga, N. (2001). Structural behavior of rice husk silica in pressurized hot-water treatment processes. *Industrial & Engineering Chemistry Research, 40*(24), 5705–5709. https://doi.org/10.1021/ie0100683

Nagpal, R., Bhardwaj, N. K., Mishra, O. P., & Mahajan, R. (2021). Cleaner bio-pulping approach for the production of better strength rice straw paper. *Journal of Cleaner Production, 318*, Article 128539. https://doi.org/10.1016/j.jclepro.2021.128539

Nam, S., French, A. D., Condon, B. D., & Concha, M. (2016). Segal crystallinity index revisited by the simulation of X-ray diffraction patterns of cotton cellulose Iβ and cellulose II. *Carbohydrate Polymers, 135*, 1–9. https://doi.org/10.1016/j.carbpol.2015.08.035

Ngoc Hong, P. (2017). Carbon nanotube and graphene aerogels – The world's 3D lightest materials for environment applications: A review. *International Journal of Materials Science and Applications, 6*(6), 277. https://doi.org/10.11648/j.ijmsa.20170606.12

Ong, E. S., Cheong, J. S. H., & Goh, D. (2006). Pressurized hot water extraction of bioactive or marker compounds in botanicals and medicinal plant materials. *Journal of Chromatography A, 1112*(1–2), 92–102. https://doi.org/10.1016/j.chroma.2005.12.052

Plaza, M., Amigo-Benavent, M., del Castillo, M. D., Ibáñez, E., & Herrero, M. (2010). Facts about the formation of new antioxidants in natural samples after subcritical water extraction. *Food Research International, 43*(10), 2341–2348. https://doi.org/10.1016/j.foodres.2010.07.036

Requena, R., Jiménez-Quero, A., Vargas, M., Moriana, R., Chiralt, A., & Vilaplana, F. (2019). Integral fractionation of rice husks into bioactive arabinoxylans, cellulose nanocrystals, and silica particles. *ACS Sustainable Chemistry & Engineering, 7*(6), 6275–6286. https://doi.org/10.1021/acssuschemeng.8b06692

Sahu, O. (2021). Characterisation and utilization of heterogeneous catalyst from waste rice-straw for biodiesel conversion. *Fuel, 287*, Article 119543. https://doi.org/10.1016/j.fuel.2020.119543

Seagaletal.,n.d.Seagal, J. J., Creely, A. E. Martin, J. Conrad, C. M. n.d.An Empirical Method for Estimating the Degree of Crystallinity of Native Cellulose Using the X-Ray Diffractometer. Textile Research Journal, 1, 786-794. https://doi.org/10.1177/004051755902901003.

Simon, M., Fulchiron, R., & Gouanvé, F. (2022). Water sorption and mechanical properties of cellulosic derivative fibers. *Polymers, 14*(14), 2836. https://doi.org/10.3390/polym14142836

Sluiter, A. (2008). *Determination of extractives in biomass: Laboratory Analytical Procedure (LAP); issue date 7/17/2005. Technical report. 12*.

Sluiter, A. (2008). *Determination of structural carbohydrates and lignin in biomass: Laboratory Analytical Procedure (LAP); Issue Date: April 2008; Revision Date: July 2011 (Version 07-08-2011). Technical Report. 18*.

Spence, K. L., Venditti, R. A., Rojas, O. J., Habibi, Y., & Pawlak, J. J. (2010). The effect of chemical composition on microfibrillar cellulose films from wood pulps: Water interactions and physical properties for packaging applications. *Cellulose, 17*(4), 835–848. https://doi.org/10.1007/s10570-010-9424-8

Sun, Y., Chu, Y., Wu, W., & Xiao, H. (2021). Nanocellulose-based lightweight porous materials: A review. *Carbohydrate Polymers, 255*, Article 117489. https://doi.org/10.1016/j.carbpol.2020.117489

Wang, X., Zhang, Y., Jiang, H., Song, Y., Zhou, Z., & Zhao, H. (2016). Fabrication and characterization of nano-cellulose aerogels via supercritical CO2 drying technology. *Materials Letters, 183*, 179–182. https://doi.org/10.1016/j.matlet.2016.07.081

Wang, Z., Qiao, X., & Sun, K. (2018). Rice straw cellulose nanofibrils reinforced poly (vinyl alcohol) composite films. *Carbohydrate Polymers, 197*, 442–450. https://doi.org/10.1016/j.carbpol.2018.06.025

Wu, Q., Yao, F., Xu, X., Mei, C., & Zhou, D. (2013). Thermal degradation of rice straw fibers: Global kinetic modeling with isothermal thermogravimetric analysis. *Journal of Industrial and Engineering Chemistry, 19*(2), 670–676. https://doi.org/10.1016/j.jiec.2012.10.026

Xiao, S., Gao, R., Lu, Y., Li, J., & Sun, Q. (2015). Fabrication and characterization of nanofibrillated cellulose and its aerogels from natural pine needles. *Carbohydrate Polymers, 119*, 202–209. https://doi.org/10.1016/j.carbpol.2014.11.041

Xie, Y., Xu, S., Xu, Z., Wu, H., Deng, C., & Wang, X. (2016). Interface-mediated extremely low thermal conductivity of graphene aerogel. *Carbon, 98*, 381–390. https://doi.org/10.1016/j.carbon.2015.11.033

Xu, F., Liu, C. F., Geng, Z. C., Sun, J. X., Sun, R. C., Hei, B. H., Lin, L., Wu, S. B., & Je, J. (2006). Characterisation of degraded organosolv hemicelluloses from wheat straw. *Polymer Degradation and Stability, 91*(8), 1880–1886. https://doi.org/10.1016/j.polymdegradstab.2005.11.002

Yang, H., Yan, R., Chen, H., Lee, D. H., & Zheng, C. (2007). Characteristics of hemicellulose, cellulose and lignin pyrolysis. *Fuel, 86*, 1781–1788. https://doi.org/10.1016/j.fuel.2006.12.013

Yang, X., & Cranston, E. D. (2014). Chemically cross-linked cellulose nanocrystal aerogels with shape recovery and superabsorbent properties. *Chemistry of Materials, 26*(20), 6016–6025. https://doi.org/10.1021/cm502873c

Yunus, R., Salleh, S. F., Abdullah, N., & Biak, D. R. A. (2010). Effect of ultrasonic pre-treatment on low temperature acid hydrolysis of oil palm empty fruit bunch. *Bioresource Technology, 101*(24), 9792–9796. https://doi.org/10.1016/j.biortech.2010.07.074

Zainuddin, S. Y. Z., Ahmad, I., Kargarzadeh, H., Abdullah, I., & Dufresne, A. (2013). Potential of using multiscale kenaf fibers as reinforcing filler in cassava starch-kenaf biocomposites. *Carbohydrate Polymers, 92*(2), 2299–2305. https://doi.org/10.1016/j.carbpol.2012.11.106

Zaman, A., Huang, F., Jiang, M., Wei, W., & Zhou, Z. (2020). Preparation, properties, and applications of natural cellulosic aerogels: A review. *Energy and Built Environment, 1* (1), 60–76. https://doi.org/10.1016/j.enbenv.2019.09.002

Zhang, W., Zhang, Y., Lu, C., & Deng, Y. (2012). Aerogels from crosslinked cellulose nano/micro-fibrils and their fast shape recovery property in water. *Journal of Materials Chemistry, 22*(23), 11642. https://doi.org/10.1039/c2jm30688c

Zhang, Z., Smith, C., & Li, W. (2014). Extraction and modification technology of arabinoxylans from cereal by-products: A critical review. *Food Research International, 14*. https://doi.org/10.1016/j.foodres.2014.05.068